ACS APPLIED MATERIALS & INTERFACES

Research Article

www.acsami.org

Aerosol-Jet-Printed, 1 Volt H-Bridge Drive Circuit on Plastic with Integrated Electrochromic Pixel

Mingjing Ha,[†] Wei Zhang,[‡] Daniele Braga,[†] Michael J. Renn,[§] Chris H. Kim,[‡] and C. Daniel Frisbie*[,†]

[†]Department of Chemical Engineering and Materials Science, University of Minnesota, 421 Washington Avenue SE, Minneapolis, Minnesota 55455, United States

[‡]Department of Electrical and Computer Engineering, University of Minnesota, 200 Union Street SE, Minneapolis, Minnesota 55455, United States

[§]Optomec, Inc., 2575 University Avenue West, St. Paul, Minnesota 55114, United States

Supporting Information

ABSTRACT: In this report, we demonstrate a printed, flexible, and low-voltage circuit that successfully drives a polymer electrochromic (EC) pixel as large as 4 mm^2 that is printed on the same substrate. All of the key components of the drive circuitry, namely, resistors, capacitors, and transistors, were aerosol-jet-printed onto a plastic foil; metallic electrodes and interconnects were the only components prepatterned on the plastic by conventional photolithography. The large milliampere drive currents necessary to switch a 4 mm^2 EC pixel were controlled by printed electrolyte-gated transistors (EGTs) that incorporate printable ion gels for the gate insulator layers and poly(3-hexylthiophene) for the semiconductor channels. Upon application of a 1 V input pulse, the circuit switches the printed EC pixel ON (red) and OFF (blue) two times in approximately 4 s. The performance of the circuit and the behavior of the individual resistors, capacitors, EGTs, and the EC pixel are analyzed as functions of the printing parameters and operating conditions.

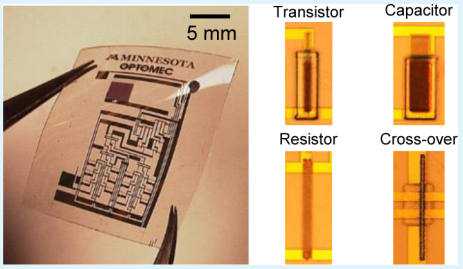

KEYWORDS: *printed electronics, flexible electronics, electrochromic pixel, transistor, capacitor, ion gel*

1. INTRODUCTION

Printing of organic integrated circuits (OICs) consisting of both active and passive electronic components (e.g., transistors and diodes vs resistors and capacitors) is a desirable goal and also a substantial challenge for the field of organic electronics.[1−5] Printing is an additive processing operation in which valuable materials are deposited only in areas where they are needed, thereby minimizing waste. Printing processes also enhance opportunities for continuous high-throughput (e.g., roll-to-roll) manufacturing and thus can benefit from economies of scale. To date, however, the quantity and complexity of OICs fabricated by printing of electronically functional inks are far below those of OICs produced by conventional photolithographic methods,[6−8] primarily because liquid-phase printing of OICs involves a range of materials engineering issues that have yet to be satisfactorily addressed, including multilayer registration, spatial resolution, materials compatibility, and reproducible control of film morphology.

Additionally, from an electrical performance perspective, it is also difficult to achieve printed OICs that operate at low voltages compatible with thin-film batteries. Achieving low-voltage operation is challenging in part because the transistor gate dielectric thicknesses must be <100 nm, perhaps as thin as 10 nm, in order to have sufficient gate capacitance for low-voltage switching. Another factor affecting the required biases is the transistor channel conductances (which are directly related to carrier mobility/channel length). High channel conductances are necessary to obtain high switching speeds at low supply biases.

In this report, we demonstrate a printed, flexible H-bridge drive circuit operating at 1 V that is fully integrated with a 2 mm × 2 mm printed polymer electrochromic (EC) pixel. Central to this demonstration is the successful printing of resistors, capacitors, and thin-film transistors (TFTs) on polyester (PET) foil. To print metals, semiconductors, and dielectrics, we employed aerosol jet printing, a technique capable of printing a wide range of electronically functional inks with line widths as narrow as 10 μm.[9,10] In order to control large drive currents at low voltages, a combination that is necessary for driving an EC pixel, we adopted electrolyte-gated transistor (EGT) technology for the TFTs.[11] EGTs produce large drive currents at low supply biases by virtue of an ultrahigh-capacitance electrolyte gate insulator layer that allows large charge densities to be induced in the EGT channels.[9,12−14] The completed circuit generates a 1 V output signal to switch the color of the printed EC pixel reversibly. Overall, the novelty of the work reported here lies in (1) the use of aerosol jet printing to produce a functional circuit containing 55 individual

Received: September 25, 2013
Accepted: November 19, 2013

   dx.doi.org/10.1021/am404204q | ACS Appl. Mater. Interfaces XXXX, XXX, XXX−XXX

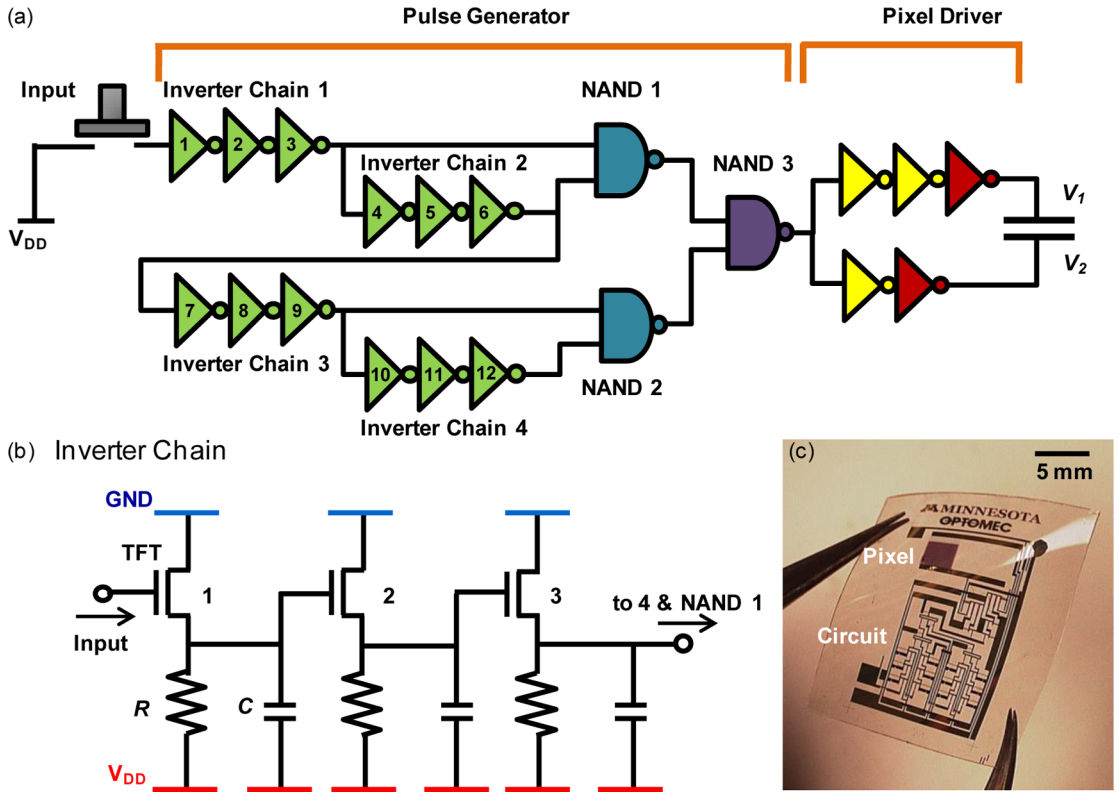

Figure 1. Flexible H-bridge drive circuit and integrated electrochromic (EC) pixel based on printed p-type electrolyte-gated transistors (EGTs), capacitors, and resistors. (a) Diagram of the driving circuit. The pulse generator, including four inverter chains (12 stages of inverters) and three NAND gates, develops two consecutive pulses with an input trigger. The pixel H-bridge driver boosts the output current in order to switch the pixel efficiently. The EC pixel, represented by a capacitor, is driven by V_1 and V_2. (b) Circuit layout of a single inverter chain consisting of three stages of inverters. Each stage employs a p-type EGT, a load resistor (R), and a load capacitor (C). After the third stage, the signal is split and goes to stage 4 and NAND 1, respectively. (c) Photograph of the printed circuit with a 2 mm × 2 mm EC display pixel on a flexible PET substrate. The entire circuit consists of 23 EGTs, 12 capacitors, 20 resistors and nine crossovers.

devices (e.g., transistors, capacitors, resistors) with good reproducibility, (2) the integration of a printed EC pixel onto the same substrate using the same printing methodology, and (3) the very low voltage operation of the complete assembly. We also show that the circuit has remarkably good operational stability with essentially no degradation in performance over 100 min of continuous operation.

It is important to note that EC displays based on electrochromic π-conjugated polymers currently represent a very active field of research.[15−20] EC displays can provide a full gamut of colors. They are simple to produce and can be integrated into a spectrum of products ranging from smart windows and mirrors to simple packaging displays.[21−24] Several groups have demonstrated active matrix control of flexible electrochromic displays.[25−27] A major concern about EC displays has generally been their switching speeds (on the order of seconds to subseconds), which are the result of relatively low ionic fluxes into or out of the electrochromic polymers upon voltage changes.[28,29] By using high-conductivity ion gels in printed EC pixels, we demonstrate efficient switching at 1 Hz, which is faster than most current demonstrations in the literature. The possibility of much faster switching on the order of 100 Hz is also discussed.

2. RESULTS AND DISCUSSION

Circuit Overview. OICs were fabricated on transparent, flexible PET substrates using the aerosol jet printing technique, which has been described previously.[9] The dimensions of the circuit elements were defined by Au contacts prepatterned by photolithography. All of the functional materials were printed. These materials included the following: poly(3-hexylthiophene) (P3HT); the ion gel,[30,31] an electrolyte composite based on the ionic liquid 1-ethyl-3-methylimidazolium bis-(trifluoromethylsulfonyl)amide ([EMI][TFSA]) and the triblock copolymer poly(styrene-*b*-methyl methacrylate-*b*-styrene) (PS−PMMA−PS); the conducting polymer PEDOT:PSS; conductive carbon nanotubes; poly(methyl methacrylate) (PMMA); and Ag.

Figure 1 illustrates the design of the entire circuit, which is composed of 23 EGTs, 12 capacitors, 20 resistors, and nine crossovers and operates with a −1 V supply. The three main components of the circuit, as shown in Figure 1a, are the pulse generator, pixel driver, and EC display pixel. Upon application of an input signal, the pulse generator, which includes four inverter (delay) chains and three NAND gates, generates two −1 V pulses. The −1 V input signal can be triggered by a function generator or by a switch connected to V_{DD}. There are three stages in each inverter chain. When the input signal passes through an inverter stage, the pulse is flipped and delayed. The delay time (t_{delay}) is a function of the RC time constant of the inverter. The more stages the signal has passed, the more delay it has compared with the original input. NAND 1 combines the signals after chain 1 and chain 2 (as labeled in Figure 1b) and produces an output pulse with a width determined by the time difference between the outputs of chain 1 and chain 2. Specifically, the pulse width is determined by $n \times t_{delay}$, where n

dx.doi.org/10.1021/am404204q | ACS Appl. Mater. Interfaces XXXX, XXX, XXX−XXX

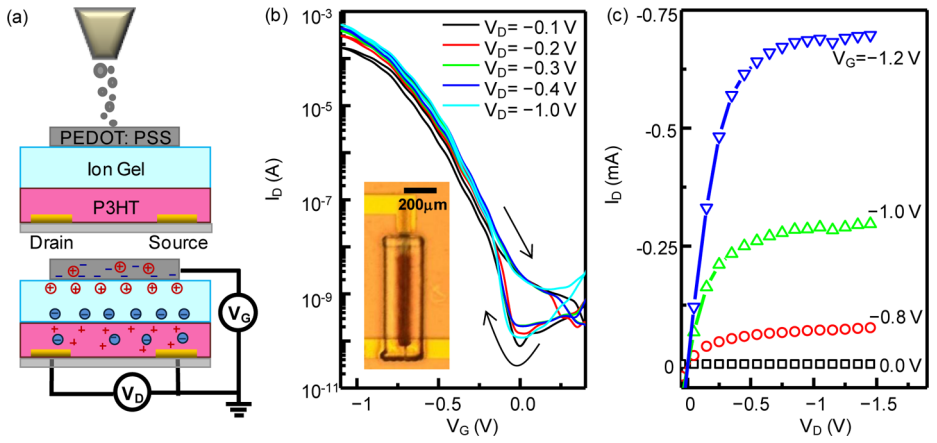

Figure 2. Printed ion-gel-gated P3HT EGTs. (a) The upper panel illustrates the stacked layer structure of the EGT printed using the aerosol jet technique. From the bottom are Au electrodes patterned on substrate, printed semiconductor P3HT, the ion gel electrolyte, and conductive gate electrode PEDOT:PSS. The lower panel illustrates the bias condition of the EGT in the ON state. With V_G and V_D < 0 V, the anions migrate to the ion gel−P3HT interface and diffuse into the bulk of the P3HT layer, which induces electrochemical oxidation of P3HT. The cations diffuse into the PEDOT:PSS layer. (b) Transfer characteristics of an EGT (W = 500 μm, L = 25 μm) at various V_D. The I_D−V_G curves were taken with V_G varying from 0.8 to −1.2 V at 75 mV/s. The inset shows a photomicrograph of a printed EGT. (c) Output characteristics at various V_G. V_D was swept at 75 mV/s.

is the number of stages in each inverter chain. This eliminates the effect of the input pulse width (i.e., the duration of pressing the switch) on the circuit output signal. Chains 3 and 4 generate a second pulse signal after NAND 2 in the same way, which is delayed in time relative to the first pulse. The two separate −1 V pulses enter NAND 3 and leave as two pulses in sequence. Simply increasing the number of inverter chains and NAND gates can increase the number of pulses (e.g., six chains and four NAND gates can generate three pulses and switch the display three times).

The two −1 V pulses after NAND 3 are sent to the H-bridge pixel driver (Figure 1a), which modulates the pulse shape and boosts the current, as is necessary to drive the pixel efficiently. The pixel driver also splits the signal and creates two separate two-pulse trains (V_1 and V_2) that are shifted in time with respect to each other by one pulse width. This ensures that when −1 V is applied to one pixel electrode, 0 V is applied to the opposite electrode; it also ensures that the direction of the applied bias flips in time. The detailed circuit diagram is shown in Figure S1 in the Supporting Information, and the signal flow of the circuit is discussed in association with Figures S2 and S3.

Figure 1b shows the component-level diagram of the first inverter chain (i.e., inverter stages 1 to 3). A typical inverter includes a p-type EGT and a load resistor, R, which are in series between ground and V_{DD}. The input signal enters the gate electrode of the EGT, and the output leaves from the node between the EGT and R. In this demonstration, we added an extra parallel capacitor, C, between V_{OUT} of the inverter and V_{DD}. The capacitor influences the charging and discharging time (i.e., the RC time) of each stage. By controlling the size of the capacitance, we can easily adjust the inverter stage delay time, t_{delay}, and thus the width of the output pulses. Additionally, the load resistors have systematically decreasing resistance across individual delay chains. This gradient change in resistance regulates the pulse shape (details are discussed in Figure S3). Large resistances are employed in the delay chains to minimize power consumption, while small resistors are used in the driver to ensure high output current for switching the EC pixel. The optical image of the drive circuit (2.5 cm × 2 cm) with an EC display (2.5 mm × 2.5 mm) printed on a PET substrate is shown in Figure 1c. The architecture and characteristics of each key circuit element are discussed in following sections.

Discrete Component Performance. *Printed EGTs.* The printed P3HT EGTs in the drive circuit have channel lengths L = 25 μm and widths W = 500 μm, except for the EGTs in the last stage of the pixel driver, which have a channel width of 2000 μm to ensure high output current. Figure 2a displays the stacked structure of a P3HT EGT. Source and drain electrodes and the circuit interconnects were prepatterned by lithography on the PET substrate. The printing sequence was P3HT semiconductor, then the ion gel gate insulator, and finally PEDOT:PSS, which served as the gate electrode. The EGT operating mechanism is shown in the lower panel of Figure 2a. Under negative gate bias, $[TFSA]^-$ anions migrate to the ion gel−P3HT interface, where electrochemical oxidation of P3HT polymer chains occurs. This switches the P3HT from insulating (OFF) to conductive (p-type ON) and increases the drain current (I_D) of the EGT by 5 orders of magnitude (Figure 2b). In electrolyte-gated devices, it is important to consider penetration of ions into the semiconductor if it is permeable. In this case, P3HT is permeable to the ionic liquid [EMI][TFSA], and thus electrochemical oxidation (hole doping) of the entire thickness of P3HT can occur if there is sufficient time for electrochemical reaction and ion diffusion. Therefore, EGTs based on ion-permeable semiconductors allow three-dimensional gating, and this in turn means very high drive currents are possible.[11,13,32] Importantly, the electrochemical oxidation process is reversible, allowing the device to be cycled between the ON and OFF states repeatedly. At the ion gel−PEDOT:PSS interface, $[EMI]^+$ cations also penetrate into the conductive polymer layer under negative bias, providing enough gate capacitance that the total series capacitance of the PEDOT/gel/P3HT stack remains very high.[33,34]

The electronic characteristics of typical EGTs were measured in an environment of N_2 and are shown in Figure 2b,c. The transfer curve in Figure 2b was acquired with the gate voltage (V_G) swept from +0.8 to −1.2 V and back at 75 mV/s. The p-channel EGT turned on at $V_G \approx 0$ V for V_D = −0.1 V (drain

dx.doi.org/10.1021/am404204q | ACS Appl. Mater. Interfaces XXXX, XXX, XXX−XXX

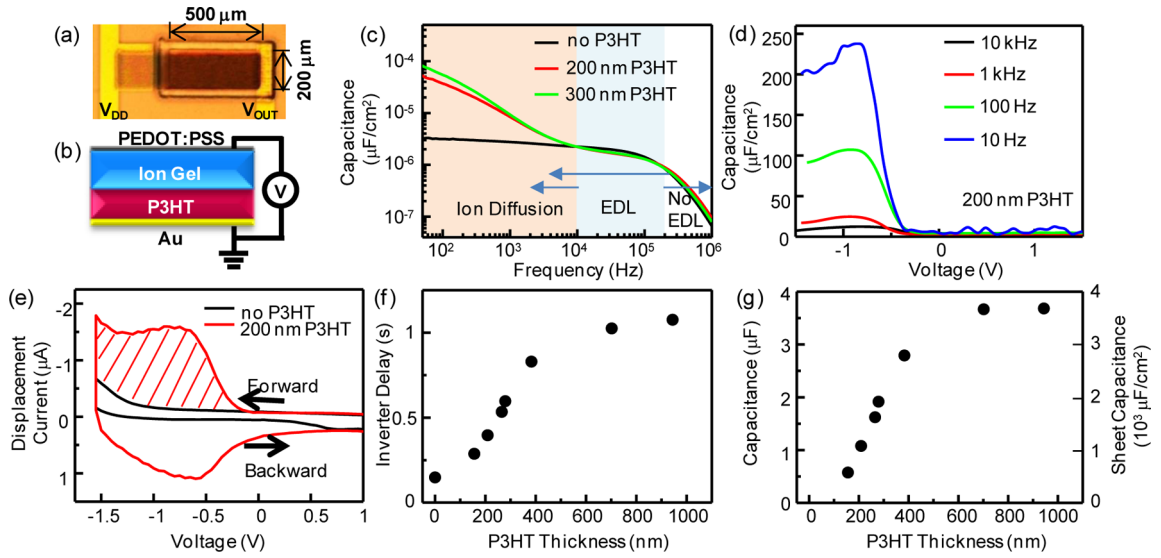

Figure 3. Printed ion gel/P3HT capacitors. (a) Photomicrograph of a printed capacitor with dimensions of 200 μm × 500 μm. P3HT and ion gel layers were printed on the Au electrode connecting to V_{OUT}. PEDOT:PSS was printed on top and extended to the electrode connecting to V_{DD}. (b) Cross section of a capacitor. (c) Capacitance–frequency (C–f) characteristics of printed capacitors with no P3HT layer (black) and P3HT layers with thicknesses of 200 nm (red) and 300 nm (green). The C–f curve can be divided into three time regimes: no EDL formation, EDL formation at the interface, and ion diffusion into the bulk polymer film. (d) Capacitance–voltage (C–V) characteristics of a printed capacitor with 200 nm thick P3HT. The capacitance increased with negative voltage ($V < -0.3$ V). (e) Displacement currents of capacitors with and without a P3HT layer. By integration of the shaded area, the effective capacitance was estimated to be 500 μF/cm^2. The voltage was swept at 2.86 V/s. (f) Delay time of the inverters with loaded capacitors. The delay time increased linearly with the P3HT thickness in the load capacitors, and saturated above 400 nm. (g) Effective capacitance of the load capacitor estimated from the delay time as a function of P3HT thickness. The estimation was based on $t = RC \ln 2$.

voltage), and the ON/OFF ratio was >10^5. Since all the devices were printed in ambient air, during printing the P3HT film was likely doped with oxygen. This resulted in slight p-doping of the P3HT layer and caused the threshold voltage (V_{th}) to shift positively.[35,36] This air-doping effect can lead to a nondesirable leakage current in the circuit at 0 V, the elimination of which would require a more complex circuit design. Instead, the printed devices were stored in rough vacuum (>10^{-3} Torr) at room temperature for 2 days in order to deoxygenate the P3HT. After it was degassed, the P3HT became less p-doped, and V_{th} shifted negatively, allowing the transistors to be turned off sufficiently at 0 V. Ideally, printing in an inert environment could eliminate oxygen doping during fabrication and thus remove the need for the deoxygenation step. The transfer I–V curves were also carefully measured with different V_D biases from −0.1 to −1 V. The ON current increased with V_D, while the turn-on voltage had weak dependence on V_D, as expected. The output curve in Figure 2c shows clear linear and saturation regimes. A photomicrograph of a printed EGT is shown in the inset of Figure 2b.

Close observation of the OFF-state current in Figure 2b reveals that the drain current in the forward sweep is about 1 order of magnitude lower than that in the backward sweep. The origin of the OFF current in the forward sweep is the parasitic capacitance in the EGT. It can be seen from the inset of Figure 2b that a small part of the source and drain electrodes are exposed to the ion gel electrolyte. This interface effectively acts as a parasitic capacitor (C_P). When V_G is swept, there is a small charging or discharging current due to this parasitic capacitor, and the current can be estimated as $I = C_P \times dV_G/dt$, where dV_G/dt is the V_G sweep rate. For the metal–ion gel interface, C_P is about 10 μF/cm^2.[13] From the sweep rate of 75 mV/s and the area of 200 μm × 100 μm, the transient current is estimated to be 1.5 × 10^{-10} A, which matches the experimental data in Figure 2b. This current can be reduced by optimizing the architecture, in particular minimizing the ion gel/source and ion gel/drain overlaps. For the reverse sweep, the dominant factor influencing the OFF current is the number of carriers remaining in the shallow trap states in the semiconductor. These traps are shallow enough that the carriers can be extracted by a slightly positive V_G. The OFF current of the consecutive forward sweep is not affected. Importantly, both the forward and reverse OFF currents are independent of the V_D bias, indicating that the static leak current through the ion gel electrolyte is very small.

Printed Capacitors. As mentioned, the total delay time, $n \times t_{delay}$, in a single delay chain determines the width of the output pulse. The number of stages, n, is not flexible once the circuit design is fixed, and t_{delay} is a function of R and C, where R is the resistance of the load resistor and C is the capacitance of the next transistor. Neither of these two factors can be tuned freely in a typical circuit.[32] Therefore, in order to tune t_{delay}, a parallel load capacitor was added in each stage of the inverter, which could be varied independently without affecting the inverter parameters. The larger the capacitor, the longer the time it took to charge and discharge, thereby increasing t_{delay}. Thus, variation of the delay time could be achieved.

Figure 3a shows a photomicrograph of a capacitor with dimensions of 500 μm × 200 μm as defined by the bottom Au electrode. The cross-sectional view of the capacitor is illustrated in Figure 3b, where P3HT and the ion gel serve as the semiconductor and insulator layers, respectively. The PEDOT:PSS top electrode connects to V_{DD}. Depending on the relative bias between the top and bottom electrodes of the capacitor, P3HT can be electrochemically oxidized or rereduced, which is loosely equivalent to the charging and discharging process of conventional capacitors. With a thicker

dx.doi.org/10.1021/am404204q | ACS Appl. Mater. Interfaces XXXX, XXX, XXX–XXX

P3HT film, there is a larger electrochemical charging capacity, and thus, a higher capacitance can be achieved.

The capacitance is reported as a function of bias frequency in Figure 3c. Without the P3HT layer, the capacitor, which is only an ion gel layer sandwiched between the PEDOT:PSS and Au electrodes, displayed $C-f$ behavior typical of a double-layer capacitor (black curve).[13] The capacitance exhibited a plateau value of ~3 μF/cm^2 for $f < 10^5$ Hz. The large capacitance derives from electrical double layer (EDL) formation at the Au−gel and PEDOT−gel interfaces. It may also reflect redox processes in the PEDOT (so-called "pseudocapacitance"). By insertion of a 200 nm P3HT layer into the capacitor, the capacitance at lower frequencies (<10^4 Hz) was significantly enhanced (red curve). The capacitance boost was a strong function of the bias frequency, as the lower frequencies allowed electrochemical oxidation to occur through the thickness of the P3HT whereas high frequencies limited the extent of oxidation. Correspondingly, the thickness of the P3HT layer also had a significant impact on the capacitance in the low-frequency regime. For instance, at 50 Hz, the capacitor with 200 nm P3HT exhibited a capacitance of 50 μF/cm^2, and another one with 300 nm P3HT displayed a capacitance of 80 μF/cm^2 (green curve). For $f > 10^5$ Hz, the capacitance decreased because EDL formation and redox reaction were suppressed.

Figure 3d displays the capacitance−voltage ($C-V$) characteristic of a capacitor with a 200 nm thick P3HT layer. With $V > -0.3$ V, the capacitance was small and weakly dependent on V. As the applied bias was swept to more negative voltages, holes were injected into P3HT, and the capacitance increased. Comparison of the $C-V$ traces at different frequencies shows that the capacitance increased at lower frequencies, consistent with the discussion above. The capacitance at 10 Hz and −1.5 V was approximately 200 μF/cm^2. However, the integrated circuits demonstrated in this report operate at frequencies of ~1 Hz. To measure the quasi-static capacitance, we recorded the capacitor displacement current (Figure 3e).[37] Charging and discharging current was measured when the voltage was swept between +1.5 V and −1.5 V at 2.86 V/s. The 200 nm P3HT capacitor (red curve) showed much higher current compared with the capacitor without P3HT (black curve). Integration of the shaded area gave a capacitance of 520 μF/cm^2, a very large value.

In order to characterize the effective capacitance of the ion-gel-gated P3HT capacitor in the drive circuit and its impact on the average delay time, t_{delay} was measured in completed circuits as a function of P3HT thickness (Figure 3f). Specifically, t_{delay} was measured from the time difference between the rising edges of two consecutive odd or even inverter stages in a delay chain (see Figure S2b). Each t_{delay} data point shown in Figure 3f was the average for 12 delay chains in which the EGTs and load resistors were the same. The value of t_{delay} for P3HT = 0 nm was acquired from inverters without load capacitors. The P3HT layer thicknesses were varied from 156 to 944 nm in the parallel load capacitors, which resulted in an increase in t_{delay} from 0.3 to 1.1 s. t_{delay} showed a transition from linear to saturation behavior at around 400 nm. With Figure 3f, we can design the thickness of the P3HT layer in capacitors on the basis of the desired delay time and pulse width. It is worth noting that t_{delay} in Figure 3f may not be quantitatively compared to the time constant of the $C-f$ measurement in Figure 3c because the charging current in Figure 3f is limited by the inverter EGT while the current in Figure 3c is limited by the impedance of the impedance analyzer. The effective capacitance can be estimated from $t_{delay}(x \text{ nm}) - t_{delay}(0 \text{ nm}) = RC \ln 2$, where R = 160 kΩ is the resistance of the load resistor in the inverter chains (see the discussion in the Supporting Information). Figure 3g shows the effective capacitance determined in this way as a function of P3HT thickness. The linearly increasing regime below 600 nm indicates that ion diffusion into P3HT leads to a sheet capacitance of roughly 10 μF/cm^2 per nanometer of P3HT layer. When the P3HT layer thickness is above 600 nm, the effective capacitance is saturated, which is likely due to the limit of ion diffusion. This limitation may be improved with better device architecture (e.g., a P3HT layer with higher porosity).

To summarize, the capacitance of the ion gel/P3HT capacitor depends on the P3HT layer thickness and the bias voltage and frequency. Thicker P3HT, higher bias, and lower frequency lead to larger capacitance, and very large specific capacitances can be obtained. It is noteworthy that the capacitance does not depend on the thickness of the ion gel insulator.

Printed Resistors and Crossovers. The load resistors in the inverter chains were made large enough (160 kΩ) to provide the required delay times and to reduce the power consumption. The resistors in NAND 1 and 2 were 80 kΩ, and in NAND 3 the value was 40 kΩ. The pixel driver employed a cascade of resistances ranging from 20 to 10 kΩ (last stage). This cascade was employed to shape the output pulse at the falling and rising edges of each stage, so that the last stage output a high-current square wave to drive the pixel (see Figure S3). Resistors were fabricated by printing PEDOT:PSS stripes between two patterned Au contacts, which fixed the length of the resistor (Figure 4a inset). The resistance depended on the thickness

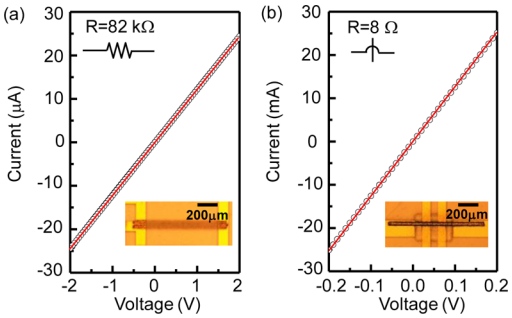

Figure 4. $I-V$ characteristics of printed resistors and crossovers. (a) $I-V$ curve of a printed PEDOT:PSS resistor (○, red line) that serves as a load resistor in NAND 1 and NAND 2 (see Figure 1). The resistance estimated from the slope is ~82 kΩ. The resistor is printed between two Au contacts, as shown in the inset. (b) $I-V$ curve of a printed crossover (○, red line). The resistance is estimated to be 8 Ω. The inset shows that a thin film of PMMA is printed on top of two vertical Au lines as the insulating layer, and a silver line is printed on top of the PMMA connecting two horizontal lines.

and width of the PEDOT:PSS stripe, which was controlled by the printing speed and number of printing passes. Figure 4a shows the $I-V$ characteristics of a typical resistor in NAND 1 and 2, and the nice linear characteristic indicates Ohmic contact between the printed PEDOT:PSS stripe and the Au pads.

It was also necessary to fabricate crossovers, or interconnects. A crossover connects two wires without shorting to others underneath. As shown in the inset of Figure 4b, a PMMA thin film was printed as a cover for the two vertical Au lines, and a line of Ag was printed on top to connect the two horizontal Au

dx.doi.org/10.1021/am404204q | ACS Appl. Mater. Interfaces XXXX, XXX, XXX−XXX

lines. The crossovers should have much smaller resistances compared with other elements in the circuit to avoid undesired voltage drops. Ag was employed because of its high conductance. The resistance of the Ag line was ~8 Ω, as assessed from the $I-V$ curve shown in Figure 4b.

Printed EC Pixel. The conjugated polymers PEDOT:PSS and P3HT are also known to be electrochromic materials with good chemical stability.[25,26,38] PEDOT:PSS is blue in the pristine or semioxidized state and transparent when further oxidized (fully conducting). P3HT has a red-purple color in the neutral state and is translucent blue when oxidized. We prepared a bicolor printed EC pixel based on the ion gel, P3HT, and PEDOT:PSS. The structure was very similar to the capacitor discussed above (Figure 3a), except that the bottom Au electrode was replaced by a printed film of conductive carbon nanotubes (CNTs), which had a high transparency to enhance the color contrast of the display pixel and enough conductance to serve as an electrode. PEDOT:PSS served as the second electrode because of its large conductance (up to 1000 S/cm). The device switched from reddish purple to blue reversibly.

Figure 5a illustrates the change in the UV−vis absorption spectrum of a stand-alone EC pixel under various voltage biases. The spectra were acquired in ambient air. The bottom conductive CNT electrode was grounded, and bias voltages of +1.5, 0, and −1.5 V were applied on the PEDOT:PSS layer. At 0 V (purple curve), the spectrum exhibited two broad absorption peaks, one in the green wavelength region (around 530 nm) due to P3HT and the other one in the near-IR region (a broad absorption around 850 nm) due to PEDOT. The positions of the two peaks are close to those in the reported absorption spectra of pristine P3HT and PEDOT:PSS, respectively.[26,39−41] At +1.5 V on PEDOT, the PEDOT:PSS layer was further oxidized compared with the 0 V condition. The near-IR absorption at 850 nm was largely suppressed (pink curve), and PEDOT:PSS turned to its transparent state. At the same time, P3HT was further reduced compared with 0 V. Since the P3HT is slightly p-doped with air exposure, this reduction brought the P3HT to its pristine state (similar to the "OFF state" in EGTs). As a result, stronger green absorption at 530 nm compared with the 0 V case can be seen. The EC pixel appeared to be purple-red at +1.5 V, as shown in the left image in Figure 5a.

At a negative bias of −1.5 V on the PEDOT:PSS electrode, PEDOT:PSS was reduced, and P3HT was oxidized. The EC pixel absorbed more at 830 nm and less at 530 nm; hence, the EC pixel exhibited a blue color, as shown in the right image of Figure 5a.

To measure the dynamic response of the printed EC pixel, the *m*-CNT electrode was grounded while a square-wave signal with controlled frequency was applied to the PEDOT:PSS electrode. A tunable light source was set to 530 and 800 nm, and the transmitted light intensities were recorded (see the Experimental Section). The detector voltage modulation of the transmission corresponding to a 1 Hz input frequency is shown in Figure 5b. The pink curve illustrates the change in the transmission at 530 nm (reflecting the change in P3HT absorption), which was maximized at V = −1.5 V and minimized at V = +1.5 V. The transmission at 800 nm (reflecting the change in PEDOT:PSS absorption), shown in the blue curve, was also modulated but in the opposite sense of the P3HT curve at 530 nm. The transmitted signals followed the modulating voltage signal, indicating that the EC pixel can fully switch at 1 Hz.

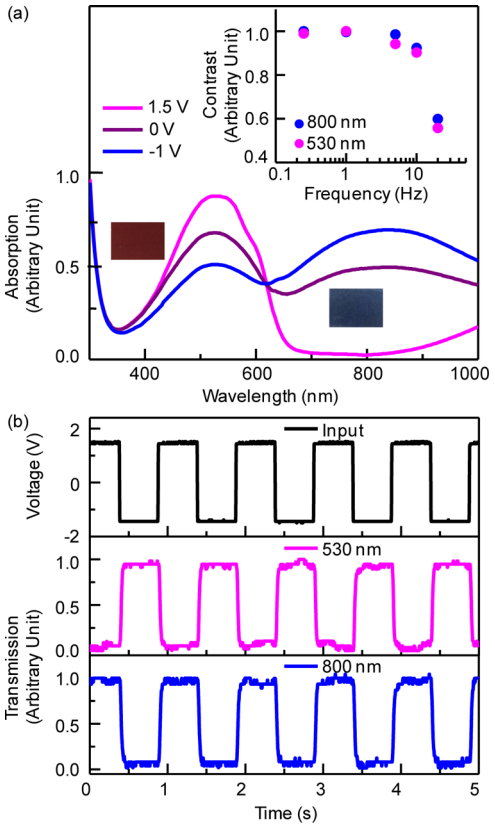

Figure 5. Characterization of printed electrochromic pixel. (a) UV−vis absorption spectra of a printed pixel under various voltage biases. At +1.5 V, the pixel has a strong absorption around 530 nm (the pristine state of P3HT) and suppressed absorption above 650 nm (the oxidized state of PEDOT:PSS). The pixel appears to be red-purple in color as shown in the left inset optical image. At −1 V, P3HT is oxidized and PEDOT:PSS is reduced; the pixel changes absorption and turns blue, as shown in the right inset optical image. The inset graph at the upper right shows the intensity contrast of a pixel as a function of bias frequency at wavelengths of 530 nm (pink) and 800 nm (blue). The y axes of both graphs are shown in normalized units. (b) Dynamic optical response of a pixel under a 1 Hz bias. The bias is shown by the black curve in the top panel, oscillating at 1 Hz, ±1.5 V. The transmitted light intensities at 530 nm (pink, middle) and 800 nm (blue, bottom) were measured. The optical response demonstrates that the pixel can fully switch at 1 Hz.

In addition, the color contrast was measured as a function of the bias frequency, as shown in the inset of Figure 5a. At each wavelength, the intensity change of the transmitted light was measured at various input voltage frequencies (0.25−20 Hz) and normalized to the change at 0.25 Hz. The EC pixel remained at full contrast up to 5 Hz. When operating at 20 Hz, the pixel produced 60% of the low-frequency contrast. Compared with EGTs and capacitors, the EC pixel is slower. This is the case because the color contrast is more sensitive to the ion diffusion depth. Full color contrast requires the electrochromic layer to be completely doped with ions. At higher frequencies, the diffusion depth of ions is limited, and thus, only part of the film changes color, resulting in the lower color contrast. On the contrary, full ion diffusion through the semiconductor layer in EGTs is not required in order to produce conductance modulation. Therefore, EGTs can function at higher frequencies of up to a few kilohertz. There is room for further optimization of the switching speed of the

dx.doi.org/10.1021/am404204q | ACS Appl. Mater. Interfaces XXXX, XXX, XXX−XXX

printed EC pixel, including modification of the device architecture, electrochromic film thickness, and electrode conductivity.

Printed Circuit Performance. Integrating all the key elements together, we demonstrate a printed EC pixel and H-bridge driver circuit in which two −1 V pulses are used to switch the pixel color two times. Since the pixel requires both polarities to switch and reset, the two outputs of the driver stage have opposite waveforms, as shown in Figure 6a. With an input trigger (black), the outputs are uniformly shaped square waves with opposite signs, where t_1 to t_4 are the delay times from inverter chains 1 to 4. The evenly distributed outputs demonstrate good control in the printing process as well as the modulation and circuit design (more details are discussed in Figure S3). The circuit operates with a −1 V supply.

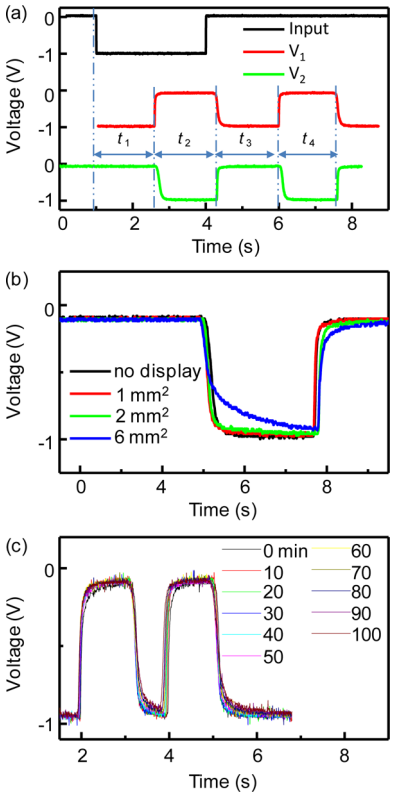

Figure 6. Output performance of the completed printed H-bridge circuit. (a) Output voltages of the printed circuit without the pixel. Triggered by the input signal (black), the circuit generates two square-wave outputs (red and green) with opposite polarity. t_1 to t_4 are determined by the delay times of inverter chains 1 to chain 4. (b) Capacity of the driving circuit. Pixels with areas of 1 and 2 mm^2 can be driven without affecting the circuit outputs. A 6 mm^2 pixel deforms the output waveform slightly because of the longer charging time. (c) Operational stability of the printed circuit. V_1 was tested continuously for 100 min (600 cycles) in N_2 and showed no degradation in output swing.

Outputs V_1 and V_2 (as labeled in Figure 1b) were connected to the PEDOT:PSS electrode and *m*-CNT electrode of the pixel, respectively. When V_1 = 0 V and V_2 = −1 V, the pixel was under −1 V bias and displayed a reddish-purple color. With V_1= −1 V and V_2 = 0 V (i.e., a flipped bias), the pixel switched to blue. The color of the display pixel switched twice upon every input pulse.

Efficient switching of EC pixels requires very large charge injection, so high output current is the key to achieving fast switching and high color contrast. The printed circuit was tested with EC pixels of different sizes ranging from 1 to 6 mm^2. A magnified view of one pixel driver output pulse as a function of the EC pixel size is shown in Figure 6b. The 1 and 2 mm^2 pixels had no obvious effects on the output signal, while the 6 mm^2 one slightly slowed down the falling edge of the drive signal, indicating that a longer time was required to switch the larger pixel. In essence, the pixel functions the same way as a load capacitor does (i.e., the capacitance and charging time increase in proportion to the area). To retain the same performance, the driving current should be proportional to the pixel size. Some simple strategies can be employed in the circuit design if larger-sized pixels are desired, such as increasing the EGT channel W/L ratio and decreasing the resistance of the load resistors in the driving unit.

We also found that the printed circuit had good operational stability. A circuit without a load pixel was tested for 100 min in N_2 continuously with V_{DD} = −1 V and an input pulse every 10 s. Output 1 was recorded every 10 min from 0 to 100 min, as shown in Figure 6c. The output signal showed excellent stability over 100 min (600 cycles) with no degradation in amplitude and only a minor shift in position.

3. CONCLUSION

In summary, we have demonstrated an aerosol-jet-printed pixel driver circuit with an integrated electrochromic pixel on plastic that operates with a −1 V supply. Key to achieving low-voltage operation was the use of electrolyte-gated transistors (EGTs) with P3HT semiconducting channels that exhibit very large gate capacitances and large drive currents. The circuit also required printed capacitors, resistors, and interconnects. The performance of these components, the EGTs, and the electrochromic pixel has been systematically analyzed. The completed circuit exhibited good stability for 100 min of continuous operation (600 input cycles). To our knowledge, this is the most sophisticated circuit based on EGTs reported to date, and it demonstrates that complex materials integration can be achieved with a simple printing process.

4. EXPERIMENTAL SECTION

Device Fabrication. The metal contacts and interconnections of the circuit were patterned by photolithography and electron-beam evaporation to form the Cr (3 nm)/Au (32 nm) electrodes on a PET substrate (Dupont). The transistor channel lengths were 25 μm, and the widths were 500 and 2000 μm.

Printing was performed under ambient conditions using a commercially available Aerosol-Jet printing system (Optomec, Inc.). During printing, the substrates were heated to 60 °C in order to dry the ink solvent. PMMA ink was printed with atomizer/sheath gas flow rates of 15/20 ccm and annealed at 160 °C for 30 min as an insulating layer for the crossovers. Then Ag nanoparticle ink (Cabot CSD-23) was printed with atomizer/sheath gas flow rates of 20/35 ccm to connect Au electrodes. The Ag layer was sintered at 150 °C for 30 min to enhance the conductivity. Conductive CNT ink for aerosol jet printing (Brewer Science) was used to pattern the bottom electrode of the EC pixel, with atomizer/sheath gas flow rates of 20/35 ccm. After the conductive CNT film was dried, the sheet resistance of the film was ~1 kΩ/sq in order to achieve a good switching speed for the pixel. Increasing the number of overlaid layers increased the conductance of the CNT film, thus enhancing the pixel switching speed. However, more layers result in lower transmittance of the CNT film and lower contrast of the EC pixel. P3HT, ion gel, and PEDOT:PSS layers were sequentially printed on the device area to fabricate transistors,

dx.doi.org/10.1021/am404204q | ACS Appl. Mater. Interfaces XXXX, XXX, XXX−XXX

capacitors, and EC pixels. P3HT (2 mg) was dissolved in 1 mL of chloroform overnight to form the P3HT ink, with 0.1 mL terpineol added as a high-boiling cosolvent before printing. The P3HT layer was printed with atomizer/sheath gas flow rates of 12/20 ccm. The ion gel ink was a mixture of 2 wt % PS−PMMA−PS (M_n = 8.9k−67k−8.9k, polydispersity = 1.17), 8 wt % [EMI][TFSA] (Merck), and 90 wt % ethyl acetate solvent. The ion gel layer was printed with atomizer/sheath gas flow rates of 10/20 ccm. Aqueous PEDOT:PSS inks [PH500 for the electrodes in the EGTs, capacitors, and the EC pixel and Clevios P VP AI 4083 for load resistors (H. C. Stark)] were diluted with 10% (v/v) ethylene glycol and printed with atomizer/sheath gas flow rates of 15/30 ccm. The printing speed for each layer varied from 2 to 5 mm/s to achieve the desired properties.

Electrical and Optical Measurements. The electrical measurements of EGTs, capacitors, resistors, and crossovers were made using two Keithley 236 source measurement units and a Keithley 6517 electrometer that were computer-controlled using Labview. The input signal of the circuit was generated by an Agilent 33220 arbitrary-waveform generator, and the output voltage was recorded by a Tektronix TDS1002B digital oscilloscope.

To measure the dynamic switching properties of the display pixel, an Oriel Cornerstone 1/8m monochromatic light source (530 or 800 nm wavelength) was employed. A chopper wheel was used to modulate the light. The light intensity transmitted through the pixel was measured by a Newport model 818-UV Low Power detector, and the measured detector current was sent to an SRS model SR810DSP lock-in amplifier. The bias voltage was applied on the pixel using the Tektronix TDS1002B digital oscilloscope. The transmission of the pixel at each wavelength was measured under different bias frequencies. Steady-state UV−vis absorption spectra of the pixel were taken on a Spectronic Genesys 5 spectrometer over a wavelength range of 300−1000 nm using a bare PET substrate as a blank.

■ ASSOCIATED CONTENT

Ⓢ Supporting Information

Circuit design and signal flow in the circuit. This material is available free of charge via the Internet at http://pubs.acs.org.

■ AUTHOR INFORMATION

Corresponding Author

*E-mail: frisbie@umn.edu.

Notes

The authors declare no competing financial interest.

■ ACKNOWLEDGMENTS

The authors acknowledge Professor Timothy P. Lodge and Keun Hyung Lee for the synthesis of the PS−PMMA−PS triblock copolymer, Dr. Yu Xia for helpful discussions, Josh Speros for help with UV−vis absorption measurements, and Professor Russell J. Holmes, Richa Pandey, and Kai Yuan Cheng for assistance with optical measurements and helpful discussions. This work was supported by the Office of Naval Research Multi-University Research Initiative (MURI) Program and a National Science Foundation CAREER Award (CCF-0845605). M.J.R. and C.D.F. also thank the Air Force for support through an STTR Grant.

■ REFERENCES

(1) Garnier, F.; Hajlaoui, R.; Yassar, A.; Srivastava, P. *Science* **1994**, *265*, 1864−1866.
(2) Berggren, M.; Nilsson, D.; Robinson, N. D. *Nat. Mater.* **2007**, *6*, 3−5.
(3) Leenen, M. A. M.; Arning, V.; Thiem, H.; Steiger, J.; Anselmann, R. *Phys. Status Solidi A* **2009**, *206*, 588−597.
(4) Someya, T. *Nat. Nanotechnol.* **2009**, *4*, 143−144.
(5) Tobjörk, D.; Österbacka, R. *Adv. Mater.* **2011**, *23*, 1935−1961.
(6) Wong, W. S.; Salleo, A. *Flexible Electronics: Materials and Applications*; Springer: New York, 2009.
(7) Nathan, A.; Ahnood, A.; Cole, M. T.; Sungsik, L.; Suzuki, Y.; Hiralal, P.; Bonaccorso, F.; Hasan, T.; Garcia-Gancedo, L.; Dyadyusha, A.; Haque, S.; Andrew, P.; Hofmann, S.; Moultrie, J.; Daping, C.; Flewitt, A. J.; Ferrari, A. C.; Kelly, M. J.; Robertson, J.; Amaratunga, G.; Milne, W. I. *Proc. IEEE* **2012**, *100*, 1486−1517.
(8) *Organic Electronics: Materials, Manufacturing and Applications*; Klauk, H., Ed.; Wiley-VCH: Weinheim, Germany, 2006.
(9) Cho, J. H.; Lee, J.; Xia, Y.; Kim, B.; He, Y.; Renn, M. J.; Lodge, T. P.; Frisbie, C. D. *Nat. Mater.* **2008**, *7*, 900.
(10) Kim, S. H.; Hong, K.; Lee, K. H.; Frisbie, C. D. *ACS Appl. Mater. Interfaces* **2013**, *5*, 6580−6585.
(11) Kim, S. H.; Hong, K.; Xie, W.; Lee, K. H.; Zhang, S.; Lodge, T. P.; Frisbie, C. D. *Adv. Mater.* **2013**, *25*, 1822−1846.
(12) Herlogsson, L.; Crispin, X.; Robinson, N. D.; Sandberg, M.; Hagel, O.-J.; Gustafsson, G.; Berggren, M. *Adv. Mater.* **2007**, *19*, 97−101.
(13) Lee, J.; Panzer, M. J.; He, Y.; Lodge, T. P.; Frisbie, C. D. *J. Am. Chem. Soc.* **2007**, *129*, 4532−4533.
(14) Herlogsson, L.; Cölle, M.; Tierney, S.; Crispin, X.; Berggren, M. *Adv. Mater.* **2010**, *22*, 72−76.
(15) Garnier, F.; Tourillon, G.; Gazard, M.; Dubois, J. C. *J. Electroanal. Chem. Interfacial Electrochem.* **1983**, *148*, 299−303.
(16) Druy, M. A.; Seymour, R. J. *J. Phys., Colloq.* **1983**, *44* (C3), C3-595−C3-598.
(17) Beaujuge, P. M.; Reynolds, J. R. *Chem. Rev.* **2010**, *110*, 268−320.
(18) Amb, C. M.; Dyer, A. L.; Reynolds, J. R. *Chem. Mater.* **2011**, *23*, 397−415.
(19) Dyer, A. L.; Thompson, E. J.; Reynolds, J. R. *ACS Appl. Mater. Interfaces* **2011**, *3*, 1787−1795.
(20) Shi, P.; Amb, C. M.; Dyer, A. L.; Reynolds, J. R. *ACS Appl. Mater. Interfaces* **2012**, *4*, 6512−6521.
(21) Rosseinsky, D. R.; Mortimer, R. J. *Adv. Mater.* **2001**, *13*, 783−793.
(22) Sonmez, G.; Sonmez, H. B. *J. Mater. Chem.* **2006**, *16*, 2473−2477.
(23) Jensen, J.; Dam, H. F.; Reynolds, J. R.; Dyer, A. L.; Krebs, F. C. *J. Polym. Sci., Part B: Polym. Phys.* **2012**, *50*, 536−545.
(24) Vasilyeva, S. V.; Beaujuge, P. M.; Wang, S.; Babiarz, J. E.; Ballarotto, V. W.; Reynolds, J. R. *ACS Appl. Mater. Interfaces* **2011**, *3*, 1022−1032.
(25) Andersson, P.; Nilsson, D.; Svensson, P.-O.; Chen, M.; Malmstrom, A.; Remonen, T.; Kugler, T.; Berggren, M. *Adv. Mater.* **2002**, *14*, 1460−1464.
(26) Andersson, P.; Forchheimer, R.; Tehrani, P.; Berggren, M. *Adv. Funct. Mater.* **2007**, *17*, 3074−3082.
(27) Yashiro, T.; Hirano, S.; Naijoh, Y.; Okada, Y.; Tsuji, K.; Abe, M.; Murakami, A.; Takahashi, H.; Fujimura, K.; Kondoh, H. *SID Int. Symp. Dig. Tech. Pap.* **2011**, *42*, 42−45.
(28) Monk, P. M. S.; Mortimer, R. J.; Rosseinsky, D. R. *Electrochromism: Fundamentals and Applications*; Wiley-VCH: Weinheim, Germany, 1995.
(29) Liu, D. Y.; Chilton, A. D.; Shi, P.; Craig, M. R.; Miles, S. D.; Dyer, A. L.; Ballarotto, V. W.; Reynolds, J. R. *Adv. Funct. Mater.* **2011**, *21*, 4535−4542.
(30) Zhang, S.; Lee, K. H.; Frisbie, C. D.; Lodge, T. P. *Macromolecules* **2011**, *44*, 940−949.
(31) Lee, K. H.; Zhang, S.; Lodge, T. P.; Frisbie, C. D. *J. Phys. Chem. B* **2011**, *115*, 3315−3321.
(32) Xia, Y.; Zhang, W.; Ha, M.; Cho, J. H.; Renn, M. J.; Kim, C. H.; Frisbie, C. D. *Adv. Funct. Mater.* **2010**, *20*, 587−594.
(33) Ueno, K.; Nakamura, S.; Shimotani, H.; Ohtomo, A.; Kimura, N.; Nojima, T.; Aoki, H.; Iwasa, Y.; Kawasaki, M. *Nat. Mater.* **2008**, *7*, 855−858.
(34) Yuan, H.; Shimotani, H.; Tsukazaki, A.; Ohtomo, A.; Kawasaki, M.; Iwasa, Y. *Adv. Funct. Mater.* **2009**, *19*, 1046−1053.
(35) Meijer, E. J.; Detcheverry, C.; Baesjou, P. J.; van Veenendaal, E.; de Leeuw, D. M.; Klapwijk, T. M. *J. Appl. Phys.* **2003**, *93*, 4831−4835.

(36) Zhuo, J.-M.; Zhao, L.-H.; Png, R.-Q.; Wong, L.-Y.; Chia, P.-J.; Tang, J.-C.; Sivaramakrishnan, S.; Zhou, M.; Ou, E. C. W.; Chua, S.-J.; Sim, W.-S.; Chua, L.-L.; Ho, P. K. H. *Adv. Mater.* **2009**, *21*, 4747−4752.
(37) Liang, Y.; Chang, H.-C.; Ruden, P. P.; Frisbie, C. D. *J. Appl. Phys.* **2011**, *110*, No. 064514.
(38) Sapp, S. A.; Sotzing, G. A.; Reddinger, J. L.; Reynolds, J. R. *Adv. Mater.* **1996**, *8*, 808−811.
(39) Chen, T.-A.; Wu, X.; Rieke, R. D. *J. Am. Chem. Soc.* **1995**, *117*, 233−244.
(40) Shrotriya, V.; Ouyang, J.; Tseng, R. J.; Li, G.; Yang, Y. *Chem. Phys. Lett.* **2005**, *411*, 138−143.
(41) Yoon, M.-H.; Yan, H.; Facchetti, A.; Marks, T. J. *J. Am. Chem. Soc.* **2005**, *127*, 10388−10395.